JOURNAL OF MATERIALS SCIENCE **38** (2003) 461–470

Strength of thermally exposed alumina fibers

Part I *Single filament behavior*

P. E. CANTONWINE*
Materials Science and Engineering Department, University of Virginia, Charlottesville, VA 22903, USA

The strength of a continuous-fiber-reinforced ceramic composite is directly related to the strength distribution of the reinforcements. Therefore, it is essential to understand how processing and service conditions affect the filament strength distribution. The objective of this paper was to determine the strength distribution of Nextel™ 610 alumina filaments, a potential reinforcement in oxide-oxide ceramic composites, and to characterize the defect population as a function of exposure temperature. The filament strength was measured in single filament tests and decreased as the exposure temperature increased. The defect population was quantified via fractography, and eight distinct defect types were identified. Grain growth and filament-to-filament sintering were identified as critical microstructural changes during the heat treatments, and both affected the development of grain boundary grooves, either from thermal etching or from the breaking of the filament-to-filament sintering bonds. The initial crack path was intergranular but quickly changed to a mixture of transgranular and intergranular fracture. During catastrophic crack growth, the crack path changed back to intergranular. The critical crack size, as calculated from linear elastic fracture mechanics, was found in many cases to be greater than the size of the strength limiting defect suggesting the presence of subcritical cracking.

1. Introduction

Improvements in oxide fibers [1–5] and the development of fiber coatings that are compatible with the fiber, the matrix, and stable in high temperature oxidizing environments [6–8] has led to interest in oxide-oxide composites. The predictions of performance limits such as maximum service temperature, environment (steam, air, etc.), and lifetime are critical for the successful development of oxide-oxide composite components. In a ceramic composite, performance degradation generally results from fiber and fiber-matrix interface degradation. The processing stage of oxide-oxide composites is of particular interest because the processing temperatures are typically higher than the application temperatures [9–11], meaning much degradation can occur prior to service. The objective of this work was to investigate the effect of processing temperatures on the strength of Nextel™ 610 alumina fibers, a potential reinforcement in oxide-oxide composites [12].

For oxide-oxide composites, degradation of fiber strength via defect creation can occur by grain growth [14], filament-to-filament sintering [15], and interface reactions [16]. Ceramics are defect sensitive materials, therefore the fracture surface may have the classic mirror, mist and hackle regions [17]. The critical defect is found by following the river lines back to the point where the crack initiated. Catastrophic failure in a perfectly brittle material[1] is predicted by relating strength to the fracture toughness (K_{IC}):

$$\sigma_u = \frac{K_{IC}}{\psi\sqrt{\pi c}} \tag{1}$$

where ψ is a function of the sample and crack geometry and c is the critical crack size.

Defects in ceramics come in many shapes and sizes. For example, in alumina internal pores [18–20], inclusions [5, 20], machining damage [21], large grains [18, 22] and spontaneous microcracking [17] have been observed as defects. Under perfectly brittle conditions and assuming the crack size is equivalent to the defect size, the strength of alumina can be predicted from Equation 1. Alumina may, however, exhibit subcritical crack growth due to grain bridging [23], environmental attack [24] or residual stresses [25].

The lack of a quantitative description of the defect evolution in the reinforcing filaments of oxide-oxide composites during processing and service has retarded the emergence of life prediction models. Here, the evolution of the defect population during processing and

[1] A perfectly brittle material has a constant resistance to fracture, therefore when Equation 1 is satisfied and the load is not decreasing, the rate of change in K is also greater than the rate of change in the resistance.

* *Present Address*: Bechtel Bettis Inc. P.O. Box 79, ZAP 14B, West Mifflin, PA 15122, USA.

their effect on strength are investigated by measuring the single filament properties of "dry" Nextel™ 610 alumina fibers as a function of thermal exposure above 1100°C. The potential existence of subcritical cracking in this small grain alumina will also be discussed. A subsequent paper focuses on the properties of alumina fiber bundles [26].

2. Experimental procedures

2.1. Materials and processing

Nextel™ 610 is 99.5% Al_2O_3 with approximately 400 filaments per tow; the filament diameter is approximately 12 μm [27]. The filaments are manufactured from an organic aluminum-salt solution. "Green" filaments are spun from a multi-orifice spinnerette, fired slowly to remove the volatiles and then converted to alpha alumina at 1400°C [27]. Before winding onto a spool the tow is coated with an organic sizing. The Nextel™ 610 fiber tow is a high-strength reinforcement used in metal and ceramic matrices [28]. The high strength is achieved by keeping the grain size small (less than 100 nm) and eliminating many of the process induced defects [28].

The effects of thermal exposure were investigated via a continuous heat-treatment process. The Nextel™ 610 was continuously drawn at 30 cm/min. through two furnaces; the line tension was around 0.7 N to avoid significant sagging. To burn off the sizing, the temperature of the first furnace was set at 750°C. The second, or sintering, furnace was set at temperatures ranging from 1100°C to 1450°C. Since, the hot zone was about 30 cm in length, the fibers were at temperature for about 1 minute. To investigate the possible introduction of handling flaws, an experiment to represent the as-received condition was done with the sintering furnace at room temperature. The final step was to resize the bundles by infiltrating a polyvinyl butyral/methanol solution into the bundles and then curing. This resizing step allowed for more uniform gripping of the filaments during the testing of the filament bundles [26].

2.2. Testing and characterization

Single filaments were extracted from the bundles and tested at room temperature using procedures described elsewhere [15, 29]. The fracture surfaces of the saved samples[2] were observed, and the filament diameters were measured in a scanning electron microscope (SEM). The failure loads were measured using an ATS series 1100 tensile testing machine with a 50 lb. load cell and a crosshead speed of 0.25 cm/min.

The grain size was measured using a line intercept method from field-emission-gun SEM photomicrographs of etched filament surfaces. For exposure temperatures greater than 1200°C, the grain boundaries were exposed by thermal etching. The other filaments were etched in boiling phosphoric acid for approximately 45 seconds. The percent of intergranular fracture (PIF) versus distance from a surface defect was determined for fibers in the as-received condition and exposed to 1400°C. The PIF near a defect was measured in an area approximately 0.2 μm × 1 μm. At all other distances, the PIF was determined for a 1 μm × 1 μm area.

3. Results

3.1. Filament strength

Filament strengths were calculated from the measured failure loads and filament diameters. The probability of failure, P_f, was determined by standard methods [30][3]:

The data were then fitted to a Weibull distribution which, ignoring small variations in filament diameters[4], can be written as:

$$P_f = 1 - \exp\left\{\frac{-L}{L_o}\left(\frac{\sigma}{\sigma_o}\right)^m\right\} \qquad (2)$$

where σ is the filament stress, σ_o and m are the Weibull reference stress and modulus, respectively. L is the test gauge length of interest, and L_o is the reference gauge length for which σ_o and m were calculated.

The Weibull modulus m was found by taking the slope of a plot of $\mathrm{Ln}(\mathrm{Ln}(1/(1-p_f)))$ versus $\mathrm{Ln}(\sigma_f)$ (see Fig. 1). The reference stress, σ_o, is the stress at $P_f = 0.63$. The Weibull parameters are given in Table I as a function of the exposure temperature. As the exposure temperature increased from 1100°C to 1450°C, the reference stress decreased by almost 25%. This decrease in σ_o also corresponded to an increase in grain size. In contrast, the Weibull modulus initially decreased from 11.0 in the as-received condition to 7.0 after exposure at 1200°C and 1300°C. When the exposure temperature increased to 1450°C, the Weibull modulus increased back to 11.0. The initial decrease in the Weibull modulus correlated to more variation in defect strength after sintering at 1300°C (Table III, discussed in Section 3.2).

Wilson [5] reported 11.5 as the Weibull modulus of the as-received Nextel™ 610 filaments and found that the average strength varied between 3.0 and 3.5 GPa. Wilson's results compare well with the strength distribution of as-received Nextel™ 610 reported herein.

Fig. 2 is a plot of the mean filament strength versus the inverse square root of grain size. Previous results for Nextel™ 610 from Xu *et al.* [14] are shown for comparison. The large increase in strength compared to Xu *et al.* was a result of improved processing procedures after 1993 [5]. The strength of Nextel™ 610 alumina fibers appear to decrease as the grain size increases. However, these strength levels are within the "Petch" branch where strength is controlled by extrinsic flaws that are larger than the grain size [31]. Thus, the decrease in strength with grain size can not be interpreted based on the Orowan analysis where failure initiates from microcracks caused by residual stress within

[2] Fractures were saved by coating the filament with petroleum jelly to dampen the energy released that often causes other locations to fail. The petroleum jelly was removed prior to making SEM observations.

[3] $P_f = \sigma - 0.5/\mathrm{N}$.

[4] The average measured diameter was 11.9 ± 1.5 μm.

TABLE I Filament strength parameters and grain size

Exposure temperature	Weibull reference stress (GPa)	Weibull modulus	Average grain size (nm)
As-Received	3.37	11.0	65 ± 6
1100°C	3.30	7.1	69 ± 7
1200°C	3.30	7.0	69 ± 8
1300°C	3.09	7.0	75 ± 8
1350°C	3.10	8.1	78 ± 9
1400°C	3.00	9.0	91 ± 11
1450°C	2.51	11.0	100 ± 15

grains. The photomicrographs in Fig. 2 show the grain size distribution for the as-received and 1450°C exposed conditions. Grain boundary groves from thermal etching were evident for exposure temperatures greater than 1200°C (1 minute exposure). The average grain size for each exposure is listed in Table I.

3.2. Defect identification

Fractography confirmed that the filament strength was controlled by extrinsic flaws. The filaments were strong enough to exhibit the classic mirror, mist and hackle surface structures, though the boundaries between each region were difficult to distinguish. By following the river lines back to the initiation site, the defects were generally found at the focal point of the mirror region. The exception was for the weld-line defects (the remnant of filament-to-filament sintering), which were slightly offset from the focal point. Eight different types of defects were identified as the cause of crack initiation and catastrophic failure (see Figs 3 and 4).

The defect types were initially classified as either internal or on the surface. Three internal defects are shown in Fig. 3: a single spherical pore, non-spherical porosity and an unidentified defect. Five different types of surface defects were observed (see Fig. 4). The

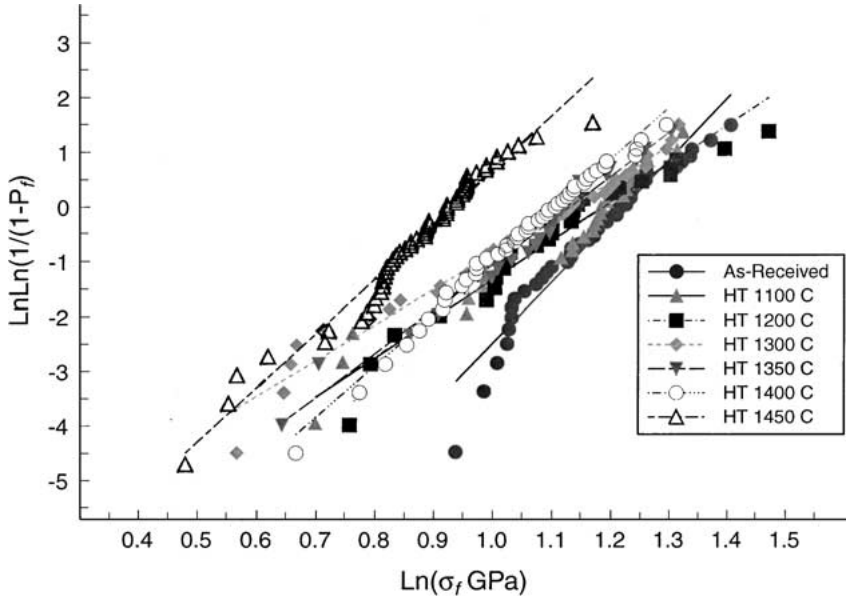

Figure 1 Plot of $\mathrm{Ln}(\mathrm{Ln}(1/P_f)$ versus $\mathrm{Ln}(\sigma_f)$. The Weibull modulus, m, is determined from the slope of these curves. Note the strength distribution is shifting to the left as the exposure temperature increases.

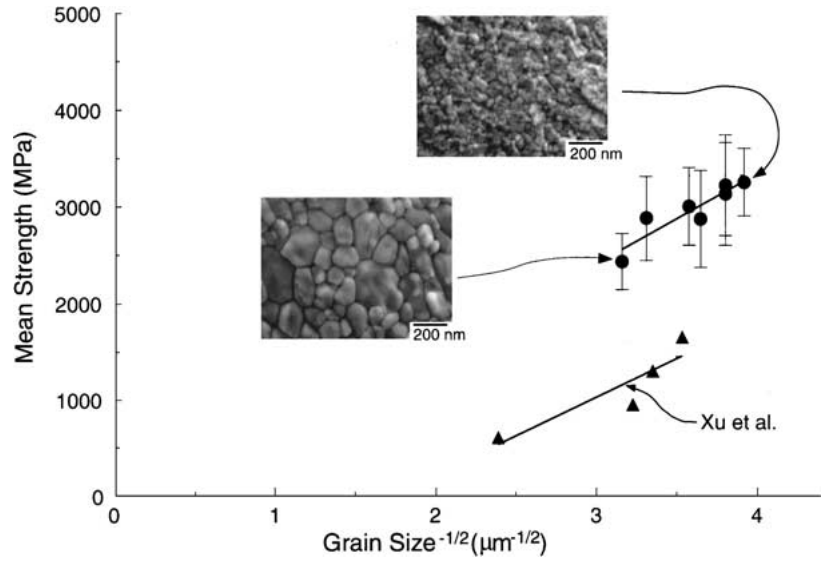

Figure 2 Mean filament strength verses the inverse square root of the grain size. The photomicrographs show the grain size distribution in the as-received condition and exposed to 1450°C for 1 minute where thermal etching caused grain boundary groves.

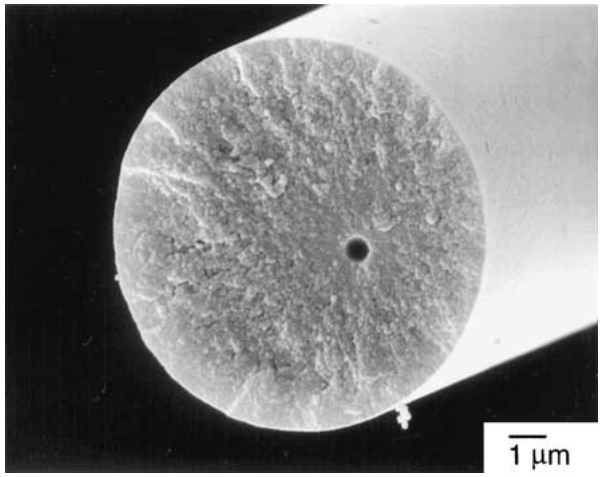

(a) Spherical Pore Defect

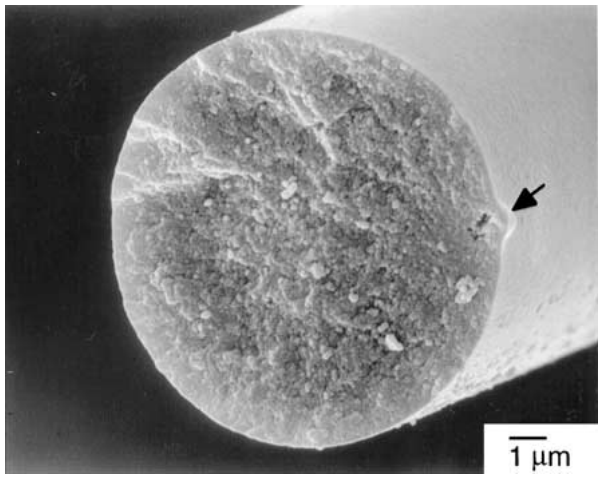

(b) Non-spherical Pore Defect

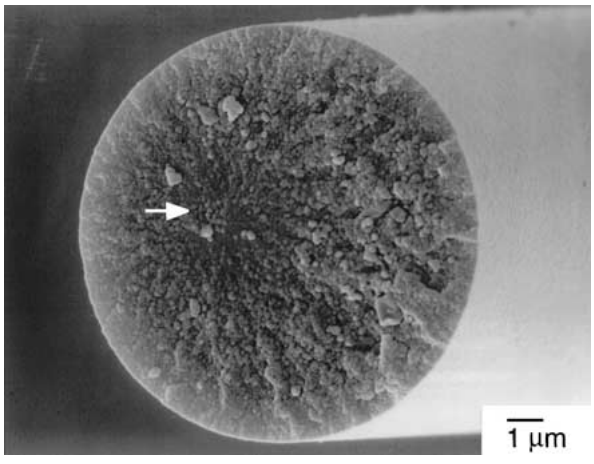

(c) Unidentified

Figure 3 Fracture surfaces of single alumina filament tests; internal defects (filament strength, diameter): (a) spherical pore (3.75 GPa, 11.1 μm) (b) non-spherical pores (3.43 GPa, 11.6 μm) and (c) unidentified (3.35 GPa, 12.2 μm).

weld-line defect shown in Fig. 4a was caused by the separation of filaments that were diffusion bonded during sintering. Fig. 4b shows an uneven surface area that was characterized as a blister defect. A surface crack is shown in Fig. 4c, and a surface nodule associated with the crack initiation site is shown in Fig. 4d. The fifth defect type was designated surface unidentified (Fig. 4e), i.e., there was no obvious geometric defect present; however, a small area of intergranular fracture was observed at the crack initiation site.

TABLE II Defect distribution in Nextel^{TM} 610 single filaments

Exposure temperature	Defect type							
	SU	SW	SC	SN	SB	IU	IP	IPY
As-received	24%	17%	–	5%	2%	14%	26%	12%
1300°C	24%	15%	12%	27%	12%	–	–	10%
1400°C	23%	33%	14%	23%	7%	–	–	–
1450°C	12%	82%	–	–	4%	–	2%	–

SU: Surface unidentified, SW: surface weld-line, SC: surface crack, SN: surface nodule, SB: surface blister, IU: internal unidentified, IP: internal spherical pore, IPY: internal non-spherical porosity.

The distribution of the defects as a function of exposure temperature is reported in Table II. The flaw population changed as the exposure temperature increased. In the as-received condition, 50% of the filaments failed from surface defects, and 50%, from internal defects. The small percentage of weld-line defects indicated that some filament-to-filament sintering occurred during the initial fiber production. These weld-line defects were approximately 0.3 μm in width and qualitatively defined as shallow, i.e., there was little evidence of grain sharing between filaments (see Fig. 5a). As the exposure temperature increased, failure from internal defects were less frequent, and the percentage of failures initiated from weld-line defects increased. The internal defects were not removed by the heat treatment, but rather, more severe, surface defects were triggered before failure at an internal defect could occur. Specifically, the weld-line defects were becoming more severe as indicated by the increased percentage of weld-line defects, which was also an indication of greater filament-to-filament sintering. After exposure at 1450°C, 82% of the filaments failed from a weld-line defect; the defect width increased to 0.5 μm, and the increased roughness was evidence of more grain sharing (see Fig. 5b). In addition, note that the weld line defect in Fig. 5b is offset from the focal point of the fracture mirror; outlined in white. The outline represents the predicted critical crack size for this filament (discussed further in Section 4.1). This offset was observed in 90% of the filaments which failed from a weld-line defect after exposure at 1450°C. The reason for this observed offset is unknown.

The average strength of each type of defect as a function of exposure temperature was determined when at least three filaments failed from that type. The strengths and standard deviations are reported in Table III. Looking at only the surface unidentified and weld-line defects, the average strength of each defect decreased with increasing temperature but were essentially equivalent after each exposure. Table II shows that the percentage of surface unidentified defects did not change significantly until after the exposure at 1450°C. The similar strengths of the weld-line and surface unidentified defects and the unchanging percentage of surface unidentified defects suggest that the actual strength limiting mechanism may be the same for these defects.

3.3. Crack path

High magnification SEM micrographs showed the cracks initiated along the grain boundaries. A spherical

TABLE III Average defect strength (GPa)

Exposure temperature	Defect type							
	SU	SW	SC	SN	SB	IU	IP	IPY
As-received	3.2 ± 0.4	3.3 ± 0.3	–	–	–	3.3 ± 0.3	3.5 ± 0.3	3.0 ± 0.3
1300°C	3.16 ± 0.4	3.15 ± 0.4	2.7 ± 0.5	3.2 ± 0.4	2.6 ± 0.4	–	–	2.6 ± 0.5
1400°C	2.85 ± 0.3	2.87 ± 0.5	2.7 ± 0.5	2.8 ± 0.2	2.87 ± 0.2	–	–	–
1450°C	2.38 ± 0.3	2.44 ± 0.4	–	–	–	–	–	–

SU: Surface unidentified, SW: surface weld-line, SC: surface crack, SN: surface nodule, SB: surface blister, IU: internal unidentified, IP: internal spherical pore, IPY: internal non-spherical porosity.

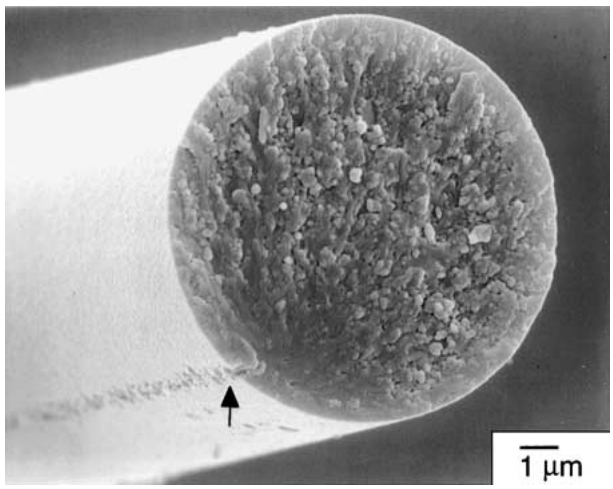

(a) Weld-Line Defect

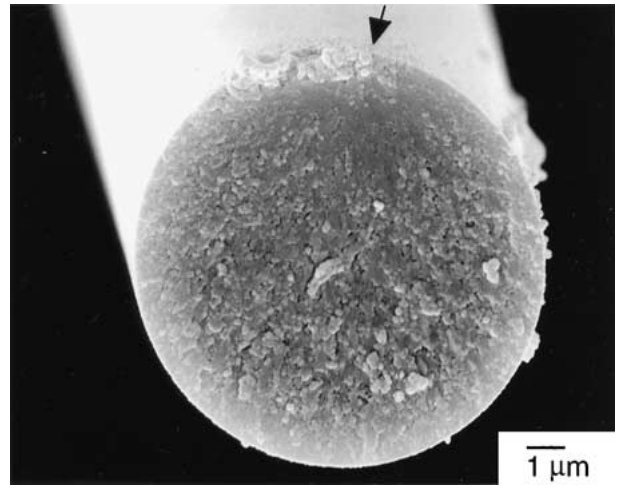

(b) Blister Defect

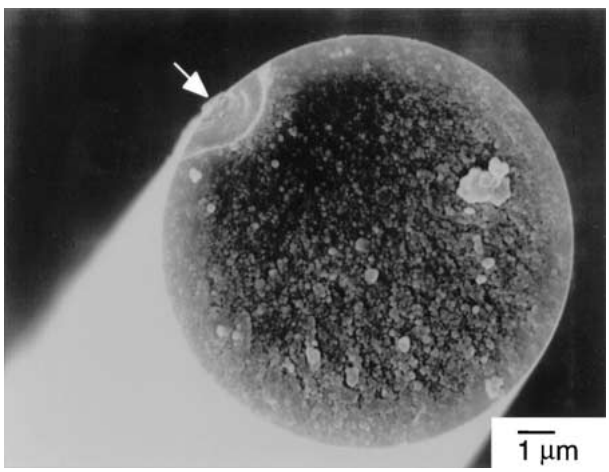

(c) Crack Defect

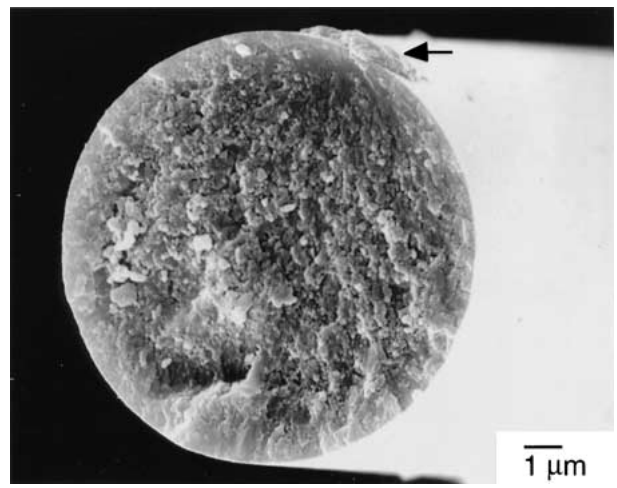

(d) Nodule Defect

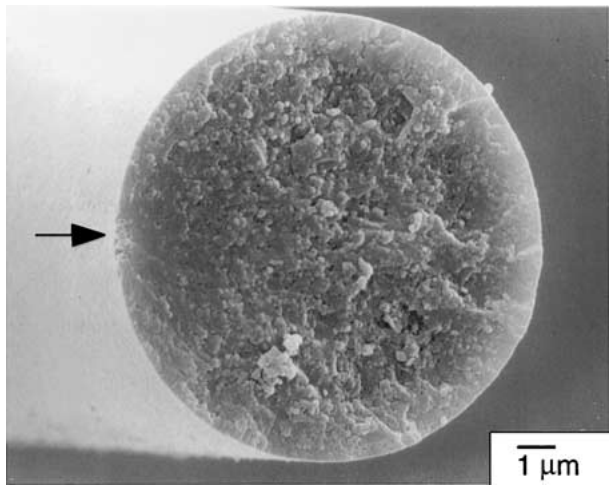

(e) Unidentified

Figure 4 Fracture surfaces of single alumina filament tests; surface defects (filament strength, diameter): (a) weld-line (2.25 GPa, 12.0 μm) (b) blister (1.91 GPa, 12.0 μm) (c) crack (1.76 GPa, 11.9 μm) (d) nodule (3.24 GPa, 13.6 μm) and (e) unidentified (3.11 GPa, 12.5 μm).

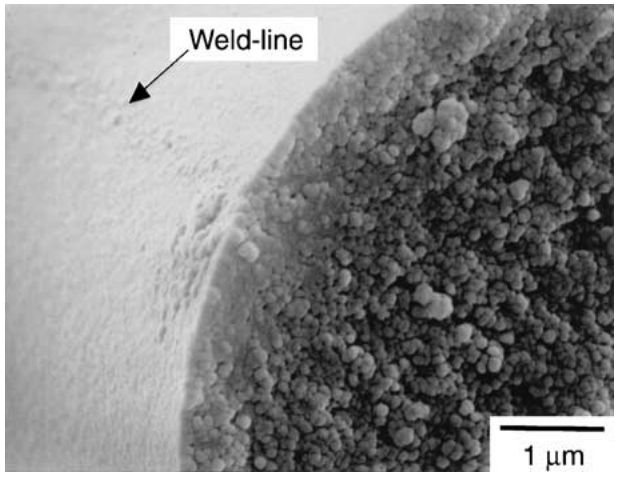

(a)

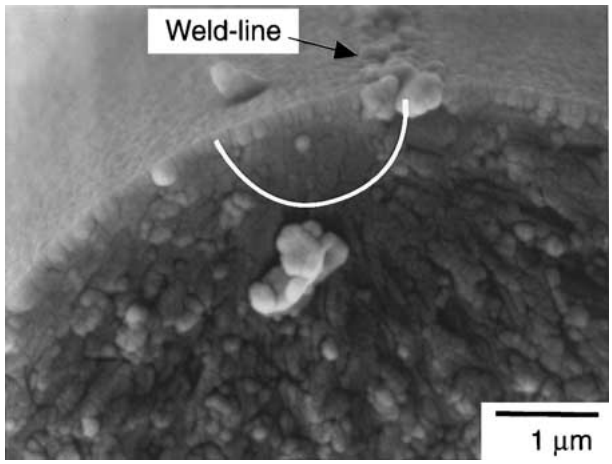

(b)

Figure 5 Weld-line defects in (a) the as-received condition (2.95 GPa); (b) exposed for 1 min. at 1450°C (2.6 GPa).

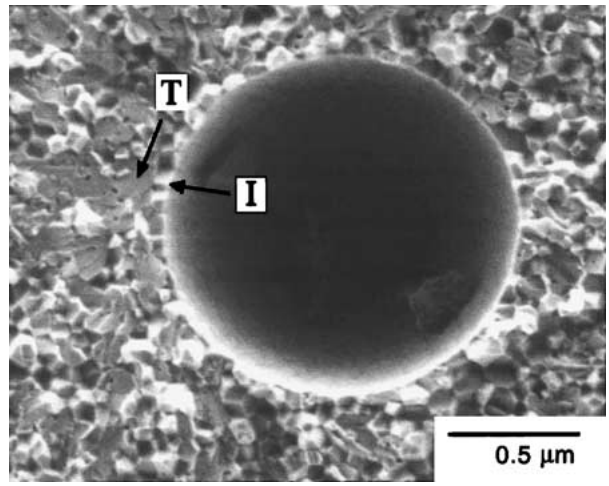

(a)

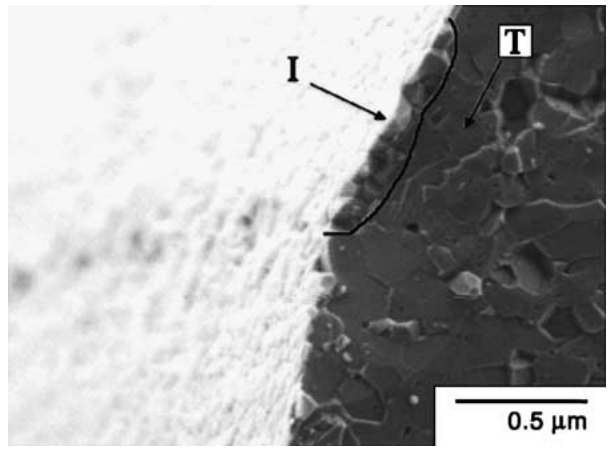

(b)

Figure 6 Crack initiation occurred along the grain boundaries: (a) an internal defect (b) a surface defect: I -intergranular fracture; T - transgranular fracture.

pore defect from an as-received filament is shown in Fig. 6a. On the left side of the defect, a ring of intergranular failure is observed that then transitions into a mixed transgranular-intergranular region. Fig. 6b is a weld-line defect from a fiber exposed at 1400°C; a small line of surface grains failed intergranularly while further propagation occurred transgranularly.

The percent of intergranular fracture (PIF) versus position from a surface defect in the as-received condition and exposed at 1400°C is shown in Fig. 7. The defect area (position 0) consisted mostly of intergranular fracture which further reinforces the observation that crack initiation occurred along grain boundaries. As the crack moved away from the defect in both fibers, the percent of intergranular fracture initially decreased and then increased. Also note that the percentage of transgranular fracture around the defected increased dramatically after the exposure to 1400°C. The observation of an increase in transgranular fracture with increasing exposure temperature was also observed by Xu *et al.* [14]

Fractography of two spherical pore defects further illustrates this last point (see Fig. 8). The first defect is from an as-received fiber where the majority of crack propagation occurs via grain boundaries except for a small region of mixed transgranular-intergranular fracture around the defect. This is compared to a fiber exposed to 1400°C (Fig. 8b) where a much larger area of transgranular fracture is observed. The transition back to intergranular fracture with increasing distance from the defect is also evident.

There were three key observations concerning the crack propagation path: (1) initiation appeared to occur along the grain boundaries around a defect; (2) as the crack propagated away from the defect, the crack path was mixed transgranular-intergranular, but eventually transitioned back to predominately intergranular fracture; (3) as the exposure temperature increased, the percent of transgranular fracture around the defect increased.

4. Discussion

In the majority of the Nextel^{TM} 610 filaments, the crack initiation site was a geometric defect while the initial crack path was along the grain boundaries. As defined in Equation 1, the strength of an alumina filament can be related to the fracture toughness, K_{IC}, the critical crack size, c, and crack geometry, ψ. The following discussion will focus largely on understanding how a critical crack evolves from a natural defect, specifically understanding the relationship between the observed defects and grain size.

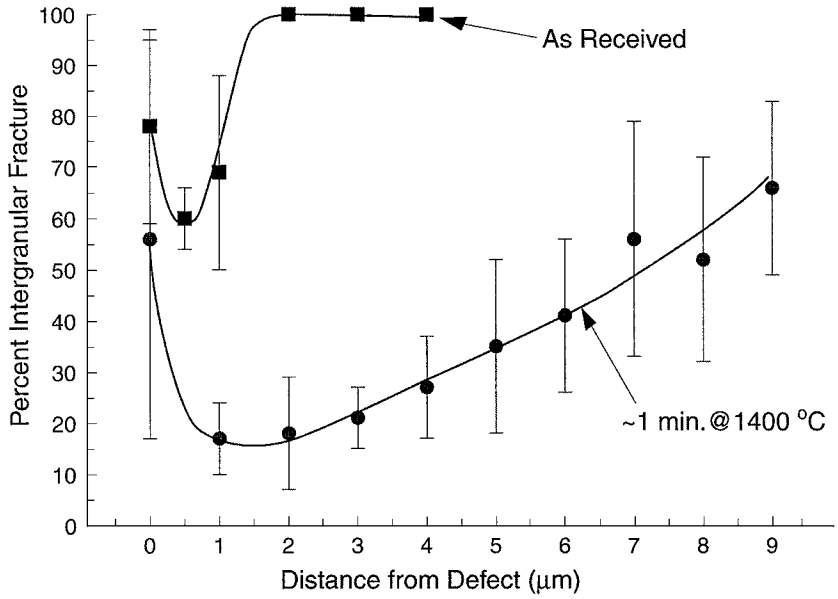

Figure 7 Percent intergranular fracture (PIF) versus position from a surface defect. The error bars represent the standard deviation of 3 measurements for the as-received samples and 5, for the 1400°C samples.

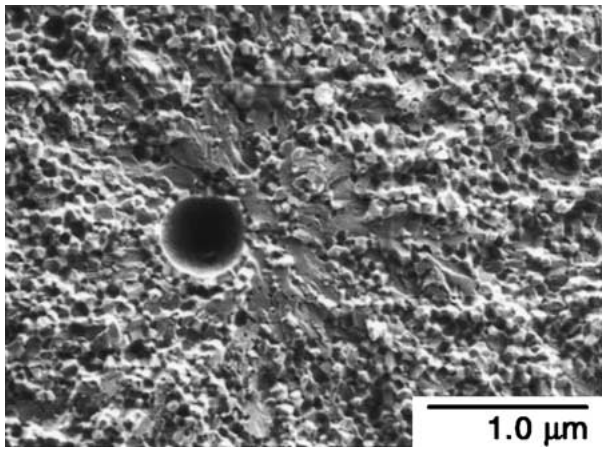

(a)

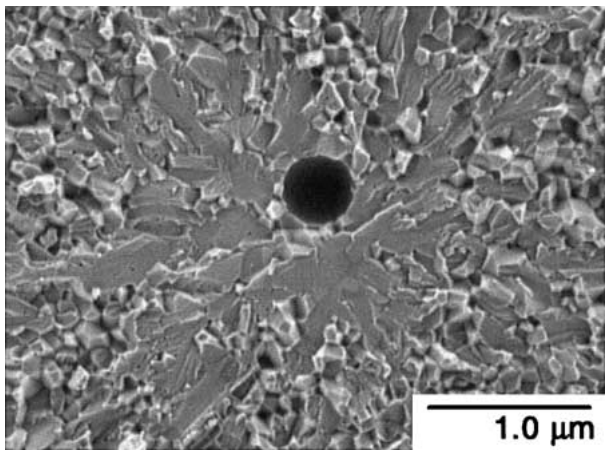

(b)

Figure 8 Spherical pore defects in filaments from (a) an as-received and (b) heat treated at 1400°C. Note that there is more transgranular fracture around the pore defect after heat treating.

4.1. Crack initiation and subcritical crack growth

The likely source of intergranular crack nucleation from surface defects and internal pores are grain boundary grooves. Grain boundary grooves from thermal etching were observed on both external (see Fig. 2) and internal surfaces [29]. Grooves were also created when separating filaments sintered together (Figs 4b, 5 and 6b). The severity of the grooves worsened as the exposure temperature increased. This was especially true for the weld-line defects (Fig. 5) which exhibited significantly more grain sharing at the higher exposure temperatures even though the width of the defects changed little (0.3 μm vs. 0.5 μm). As noted previously, the strength of the weld-line and surface unidentified defects were essentially equivalent regardless of the exposure temperature (see Table III). Since the initial fracture path is intergranular, the common link between the two defects may be the depth of the grain boundary grooves.

Once a sharp crack initiated, either subcritical or catastrophic crack growth occurred. Kurchner and Gruver in a series of papers on alumina [18, 19, 22, 32], correlated the transgranular fracture around defects to subcritical crack growth. Similar to the results of this work, they found that in weak samples a large area of transgranular fracture surrounded the critical defect while in higher strengths samples, the area of transgranular fracture was small [19]. Their theoretical calculations of the critical crack sizes were significantly larger than the observed defects, supporting the hypothesis of subcritical crack growth [19, 22, 32].

Using a similar fractography approach to determine the presence of subcritical crack growth in Nextel^{TM} 610, the critical crack sizes were calculated for a number of filaments using Equation 1 and assuming $K_{IC} = 2.75$ MPa m$^{-1/2}$ [23].[5] The crack was assumed to be semi-circular with ψ equal to 0.66 [33, 34]. The critical semi-circular crack is overlaid in white on two fracture surfaces from as-received filaments (Fig. 9); the overlay size is based on SEM magnification.

[5] Kurchner and Gruver [22] used $K_{IC} \sim 4$ MPa m$^{1/2}$ for calculating critical crack size in 1–3 μm hot-pressed alumina. In contrast, Chantikul *et al.* [23] found that K_{IC} was approximately 2.75 MPa m$^{1/2}$ for 2.5 μm alumina. The lower value appears to be more appropriate for the Nextel^{TM} 610 alumina filaments.

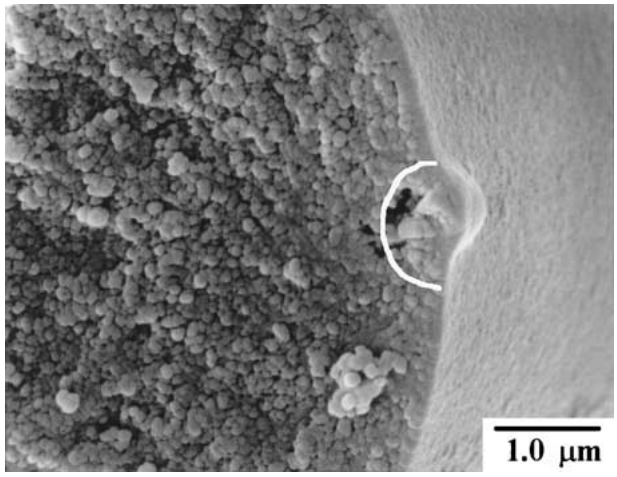

(a)

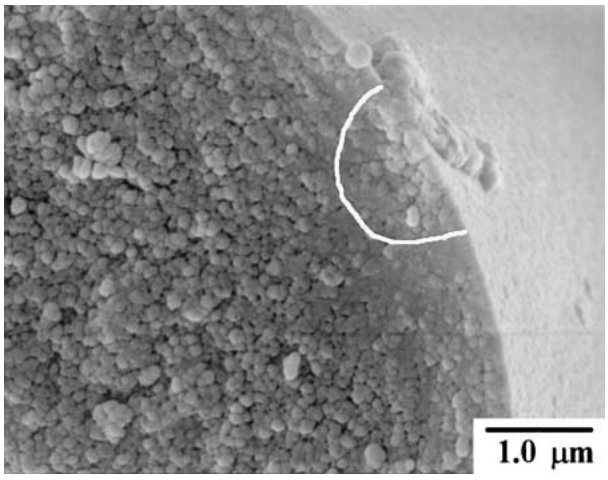

(b)

Figure 9 Crack initiation sites for two as-received filaments; (a) near-surface non-spherical defect (3.43 GPa) and (b) surface nodule defect (2.79 GPa). The outline in white represents the predicted critical crack size.

In the high strength filament, a crack initiated at an internal, non-spherical pore near the surface; close enough to assume a semi-circular surface crack. The calculated critical crack size was 0.5 μm, which matches the observed defect size. This is evidence that $K_{IC} = 2.75$ MPa m$^{-1/2}$ is a reasonable assumption. For the lower strength filament, the predicted crack size was 0.7 μm. In this lower strength filament, a crack likely initiated in the surface nodule at a low stress, subsequently propagating into the filament. Therefore, the crack must have grown subcritically. Similar conclusions were seen for other defects in low strength filaments. For example, the critical crack size around the weld-line defect in Fig. 5b was 0.8 μm. It is outlined in white to show how much larger it is compared to the observed defect.

4.2. Mechanisms of subcritical cracking

One mechanism often associated with subcritical cracking in alumina results from environmental attack at the crack tip [35, 36]. This attack lowers the intrinsic toughness of the material at the crack tip creating the rising T-Curve (or R-Curve) necessary for subcritical cracking. When environmentally assisted subcritical cracking occurs, strain-rate effects are expected [24]; the strength is expected to increase with increasing strain-rate. These strain rate effects result from the rate dependence of the environmental attack [17]. Filament strength was measured for three different strain-rates (10^{-5}/s, 10^{-4}/s, and 10^{-3}/s: room humidity, 40–50%) [29]. There was no observed effect of strain rate on strength, thus the environmental mechanism was excluded as a possibility.

Subcritical cracking can also occur for cracks in the presence of residual stresses [17, 25]. These residual stresses arise from anisotropy of the coefficient of thermal expansion [17] or elastic anisotropy between grains [37]. To better understand the effects of thermal expansion and elastic anisotropy stresses, first consider the stresses intensity around the crack tip due to only the applied stress. The stress ahead to the crack-tip can be related to the applied stress intensity factor, K_I (mode I), via [38].

$$\sigma_z = \frac{K_I}{\sqrt{2\pi y}} f(\theta) \tag{3}$$

where y is the radial distance from the crack tip and $f(\theta)$ is a function of the angle, θ, from the crack plane: $f(\theta) = \cos(\theta/2)[1 + \sin(\theta/2)\sin(3\theta/2)]$, $f(0^\circ) = 1$. The applied stress intensity factor is:

$$K_I = \sigma_A \psi \sqrt{\pi c} \tag{4}$$

where σ_A is the applied stress.

The intersection of σ_z and σ_A is the boundary of the stress intensity region and is represented by the distance, $y^* = \psi^2 c/2$. Plots of y^* as a function of the crack length, c, are shown in Fig. 10 for a semi-circular surface crack. The shaded area represents the average grain size of the as-received and exposed Nextel^{TM} 610 filaments. For crack sizes within this shaded area and below, the region of stress enhancement is contained within single grains. For the semi-circular crack, the crack length can be as much as 0.5 μm before the stress intensity encompasses multiple grains. Since these crack lengths are similar to the predicted critical crack size, the initial crack growth must be affected by the stress state within single grains.

The predicted thermal stress in 100 nm grain size alumina is about 100 MPa [39] and the effect of elastic anisotropy has been shown to be less than the thermal expansion anisotropy [40]. However, the residual thermal stresses are predicted to increase significantly as grain size increases from 60 nm to 100 nm [39], which could help explain the trends of lower strength and greater subcritical cracking with increasing grain size.

Another potential cause of the subcritical cracking is grain bridging, which results in rising T-curve behavior in alumina [17, 23]. Chantikul *et al.* [23] predicted rising T-curves for alumina with grain sizes varying from 2.5 to 80 μm. As the grain size decreased, the region of T-curve behavior decreased. Whereas the 80 μm alumina exhibited a rising T-curve at crack sizes on the order of 10 to 20 times the grain size, the rising T-curve in the 2.5 μm alumina occurred over crack sizes 1 to 3 times the grain size. Since the grain size in the Nextel^{TM}

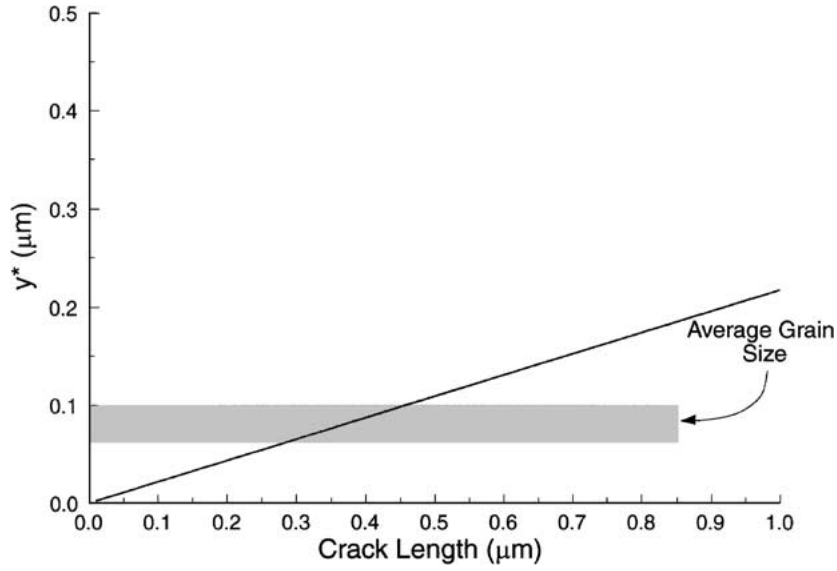

Figure 10 The stress intensity depth as a function of crack length for a semi-circular surface crack. The shaded area represent the average grain size of the as-received and thermally exposed filaments.

610 was less than 0.1 μm, the grain bridging affect will likely be small but cannot be entirely discounted.

An alternative explanation may be related to the differences between the predicted and measured intrinsic toughness, T_o, of alumina. The predicted T_o is a function of only the energy required to create new surfaces and is between 0.9 and 1.5 MPa$\sqrt{\text{m}}$[6]. In contrast, the measured T_o is between 2.5 and 3 MPa$\sqrt{\text{m}}$ [17, 23, 41, 42] and was assumed to be 2.75 MPa$\sqrt{\text{m}}$ for the calculations of the critical crack size. Since the measurements of T_o were made on samples with relatively long cracks compared to this work, there may be a scaling effect on the intrinsic toughness. The resistance to crack growth over the first few hundred nanometers may only be surface generation (i.e. $T_o = 0.9$ to 1.5 MPa$\sqrt{\text{m}}$). Then as the crack grows, other mechanisms such as additional fracture surface area from meandering cracks through grain boundaries or ledges may cause the intrinsic toughness to increase. The effect could create a rising T-curve as the crack grows from the microstructural scale to the continuum scale.

4.3. Catastrophic crack growth

Catastrophic or unstable crack growth occurs when the crack extends past the critical crack size and the rate of change in stress intensity factor with crack growth is greater than the rate of change in toughness. As the crack grows catastrophically, the region of stress enhancement ahead of the crack-tip, as defined by y^*, increases.

The mist and hackle surface structures are a result of crack branching. Crack branching dissipates excess kinetic energy via the creation of additional fracture surfaces [17]. One possible explanation of how crack branching occurs, first proposed by Yoffe [45], is that the stress field around the crack tip distorts as the velocity of the crack increases. In particular, calculations by Erdogan [46] indicated that as the velocity increased, the maximum local tensile stress moved from the perpendicular plane ($\theta = 0^\circ$) to as much as 50–70° from perpendicular. In addition as the crack size increases, y^* will encompass more grains and grain boundaries. The addition of more grain boundaries in the stress enchanced region provides more weaker boundaries for crack branching, further enhancing the crack branching due to the transition from the maximum tensile stress at $\theta = 0^\circ$ to $\theta = 50^\circ$–70°. This would help explain the transition back to intergranular fracture as the distance from the defect increased (Fig. 7).

4.4. Speculations on the effects of filament coatings for Nextel^{TM} 610

Filament coatings can have two beneficial effects, both of which inhibit the evolution of grain boundary grooves. First, a coating acts as a barrier to filament-to-filament sintering, eliminating the weld-line defects. Second, a coating will generally inhibit thermal etching. Thermal etching results from surface diffusion of atoms away from grain boundaries. In the presence of a coating, the atoms from fiber-grain boundaries must either diffuse along the filament-coating interface or through the volume. Both of these processes are generally more difficult than surface diffusion. In addition, atoms from the coating would have to diffuse toward the grain boundary to maintain compatibility. In this way the slowest diffusing species would limit the rate of thermal grooving.

Coatings also can degrade filament strength by either decreasing grain boundary energy, acting as an agent for stress corrosion cracking or having a lower failure strain compared to the filament. With better knowledge of the effect of coatings on the single filament and bundle strength (specifically identifying the crack initiation sites in coated filaments), the effect on potential matrix materials ultimately may be better understood.

5. Conclusions

The strength of Nextel^{TM} 610 alumina filaments was found to decrease as the exposure temperature

[6] The surface energies of various crystallographic planes in alumina have been reported to be from 1–3 J/m^2 [43, 44].

increased. This correlated to a change in the defect population and grain growth. Internal defects, which were observed in the as-received filaments, rarely contributed to failure after thermal exposure for ~1 minute at 1300°C. Weld-line defects caused by the breaking of filament-to-filament bonds became more prevalent as the exposure temperature increased. However, it was observed that the strength of filaments with weld-line and surface unidentified defects was essentially equivalent at all exposure temperatures. This evidence points to a common microstructural feature (likely grain boundary grooves) playing a critical role in controlling strength.

The initial crack path from the strength-limiting defect was intergranular. Subsequent propagation occurred via a mixed transgranular-intergranular path with the amount of transgranular fracture increasing as the exposure temperature increased (i.e., as the mean strength of the filaments decreased). Evidence of subcritical cracking was obtained in the lower strength filaments via fractography. The cause of the subcritical cracking is believed to be associated either with stresses induced from thermal anisotropy within the alumina, with a rising T-curve behavior in the short crack regime due to an increase in the intrinsic toughness with crack length, or less likely, to grain bridging.

During catastrophic crack propagation, the crack path transitioned back to intergranular. Two possible explanations for this transition were identified: (1) As the crack velocity increases, the maximum local tensile stress moves 50° to 70° away from the direction of the applied stress [46]. (2) The stress intensity region ahead of the crack tip increases from the size of a single grain at the onset of catastrophic failure to encompass many grains (and grain boundaries) as K_I increases.

Acknowledgements

The author is grateful to H.N.G. Wadley for servings as dissertation advisor for this work. The author also appreciates the many helpful discussions with D. Elzey, C. Herakovich and D. Wilson and practical assistance with the experimental work from P. Schare, T. Eanes and W. Shoupe. This work was supported by an AFOSR-URI grant #F49620-93-1-0359.

References

1. M. M. VOGEL-MARTIN and D. M. WILSON, in Proceedings from the 16th Conference on Metal Matrix, Carbon and Ceramic Matrix Composites, NASA Conference Publication 3175, part 2 (1992) p. 519.
2. D. WILSON, D. C. LUENEBURG and S. L. LIEDER, *Ceram. Eng. Sci. Proc.* **14** (1993) 609.
3. D. WILSON, S. L. LIEDER and D. C. LUENEBURG, in "Intermetallic Matrix Composites III," edited by J. A. Graves, R. R. Bowman and J. J. Levendoski, MRS proceedings, Vol. 350 (1994) p. 89.
4. *Idem.*, *Ceram. Eng. Sci. Proc.* **16** (1995) 1005.
5. D. WILSON, *J. Mater. Sci.* **32**(10) (1997) 2535.
6. P. E. D. MORGAN and D. B. MARSHAL, *Mat. Sci. Engr.* A **162** (1993) 12.
7. *Idem.*, *J. Amer. Ceram. Soc.* **78**(6) (1995) 1553.
8. R. W. GOETTLER, S. SAMBASIVAN and V. P. DRAVID, *Ceram. Eng. Sci. Proc.* **18**(3) (1997) 279.
9. T. A. PARTHASARATHY, E. BOAKYE, M. K. CINIBULK and M. D. PETRY, *J. Amer. Ceram. Soc.* **82**(12) (1999) 3575.
10. C. G. LEVI, J. Y. YANG, B. J. DALGLEISH, F. W. ZOK and A. G. EVANS, *ibid.* **81**(8) (1999) 2077.
11. K. A. KELLER, T. MAH, T. A. PARTHASARTHY and C. M. COOKE, *ibid.* **83**(2) (2000) 329.
12. V. A. KRAMB, R. JOHN and L. P. ZAWADA, *ibid.* **82**(11) (1999) 3087.
13. L. U. J. T. OGBUJI, *ibid.* **81**(11) (1998) 2777.
14. Z. R. XU, K. K. CHAWLA and X. LI, *Mat. Sci. Engr.* A **171**(1/2) (1993) 249.
15. P. CANTONWINE and H. WADLEY, in Advanced Ceramic-Matrix Composites IV, Proceedings from The American Ceramic Society Annual Meeting (1999) p. 51.
16. J. B. DAVIS, J. P. A. LOFVANDER, A. G. EVANS, E. BISCHOFF and M. L. EMILIANI, *J. Amer. Ceram. Soc.* **76**(5) (1993) 1249.
17. B. LAWN, in "Fracture of Brittle Solids" (Cambridge University Press, 1993).
18. R. M. GRUVER, W. A. SOTTER and H. P. KIRCHNER, *Ceram. Bull.* **55**(2) (1976) 198.
19. H. P. KIRCHNER, R. M. GRUVER and W. A. SOTTER, *Mat. Sci. Engr.* **22** (1976) 147.
20. G. K. BANSAL, W. H. DUCKWORTH and D. E. NIESZ, *J. Amer. Ceram. Soc.* **59**(11/12) (1976) 472.
21. R. E. TRESSLER, R. A. LANGENSIEPEN and R. C. BRADT, *ibid.* **57**(5) (1974) 226.
22. H. P. KIRCHNER and R. M. GRUVER, *J. Mater. Sci.* **14** (1979) 2110.
23. P. CHANTIKUL, S. J. BENNISON and B. R. LAWN, *J. Amer. Ceram. Soc.* **73**(8) (1990) 2419.
24. A. G. EVANS, *Int. J. Fracture* **10**(2) (1974) 251.
25. D. B. MARSHALL, A. G. EVANS, B. T. KHURI YAKUB, J. W. TIEN and G. S. KINO, *Proc. R. Soc. Lond.* A **385** (1983) 461.
26. P. E. CANTONWINE, *J. Mat. Sci.* **38** (2003) 471.
27. M. M. VOGEL-MARTIN and D. M. WILSON, in Proceedings from the 16th Conference on Metal Matrix, Carbon and Ceramic Matrix Composites, NASA Conference Publication 3175 part 2 (1992) p. 519.
28. D. WILSON, personal communication.
29. P. E. CANTONWINE, Ph.D. dissertation, University of Virginia, August 1999.
30. J. D. SULLIVAN and P. H. LAUZON, *J. Mater. Sci. Lett.* **5** (1986) 1245.
31. R. W. RICE, *J. Mater. Sci.* **32** (1997) 1673.
32. H. P. KIRCHNER and R. M. GRUVER, *J Amer. Ceram. Soc.* **63**(3/4) (1980) 169.
33. H. NISITANI and D. H. CHEN, *Trans Japan Soc. Mech. Engrs.* **50**(453) (1984) 1077.
34. Y. MURAKAMI, in "Stress Intensity Factors Handbook" Vol. 2 (Pergamon Press).
35. S. M. WEIDERHORN, in "Mechanical and Thermal Properties of Ceramics," edited by J. B. Wachtman, Jr., N.B.S. Special Publication 303 (1969) p. 217.
36. *Idem.*, *J. Amer. Ceram. Soc.* **50** (1967) 407.
37. V. TVERGAARD and J. W. HUTCHINSON, *ibid.* **71**(3) (1988) 157.
38. T. L. ANDERSON, in "Fracture Mechanics: Fundamentals and Applications," 2nd ed. (CRC Press, 1995).
39. Q. MA and D. R. CLARKE, *J. Amer. Ceram. Soc.* **77**(2) (1997) 298.
40. R. W. RICE, *J. Mater. Sci.* **19** (1984) 1267.
41. R. F. COOK, E. G. LINIGER, R. W. STEINBRECH and F. DEUERIER, *J. Amer. Ceram. Soc.* **77**(2) (1994) 303.
42. M. STECH and J. RODEL, *ibid.* **79**(2) (1996) 291.
43. I. MANASSIDIS and M. J. GILLAN, *ibid.* **77**(2) (1994) 335.
44. S. M. WIEDERHORN, *ibid.* **52**(9) (1969) 487.
45. E. H. YOFFE, *Phil. Mag.* **42** (1951).
46. F. ERDOGAN, in "Fracture," edited by H. Liebowitze, Vol. 2 (Academic, New York) ch. 5.

Received 11 March
and accepted 8 July 2002